Surface & Coatings Technology 377 (2019) 124853

Contents lists available at ScienceDirect

Surface & Coatings Technology

journal homepage: www.elsevier.com/locate/surfcoat

Characterisation of a High-Power Impulse Magnetron Sputtered C/Mo/W wear resistant coating by transmission electron microscopy

Jo Sharp[a,*], Itzel Castillo Müller[a], Paranjayee Mandal[c,1], Ali Abbas[b], Magnus Nord[d,2], Alastair Doye[d], Arutiun Ehiasarian[c], Papken Hovsepian[c], Ian MacLaren[d], W. Mark Rainforth[a]

[a] Department of Materials Science and Metallurgy, University of Sheffield, Sir Robert Hadfield Building, Mappin Street, Sheffield S1 3JD, UK
[b] Department of Materials, Loughborough University, Loughborough LE11 3TU, UK
[c] Materials and Engineering Research Institute, Sheffield Hallam University, City Campus, Howard Street, Sheffield S1 1WB, UK
[d] School of Physics and Astronomy, University of Glasgow, Glasgow G12 8QQ, UK

ARTICLE INFO

Keywords:
HIPIMS
Fluctuation electron microscopy
FEM
EELS
TEM
STEM

ABSTRACT

Thin films of C/Mo/W deposited using combined UBM/HIPIMS sputtering show 2–8 nm clusters of material richer in Mo and W than the matrix (found by EDS microanalysis), with structures that resemble graphitic onions with the metal atoms arranged regularly within them. EELS microanalysis showed the clusters to be rich in W and Mo.

As the time averaged power used in the pulsed HIPIMS magnetron was increased, the clusters became more defined, larger, and arranged into layers with amorphous matrix between them. Films deposited with average HIPIMS powers of 4 kW and 6 kW also showed a periodic modulation of the cluster density within the finer layers giving secondary, wider stripes in TEM. By analysing the ratio between the finer and coarser layers, it was found that this meta-layering is related to the substrate rotation in the deposition chamber but in a non-straightforward way. Reasons for this are proposed. The detailed structure of the clusters remains unknown and is the subject of further work.

Fluctuation electron microscopy results indicated the presence of crystal planes with the graphite interlayer spacing, crystal planes in hexagonal WC perpendicular to the basal plane, and some plane spacings found in Mo_2C. Other peaks in the FEM results suggested symmetry-related starting points for future determination of the structure of the clusters.

1. Introduction

In many industries, wear-resistant coatings are important to increase efficiency, lifetime and performance of moving contact parts. Diamond-like carbon (DLC) coatings, deposited by magnetron sputtering or CVD, display impressively low coefficients of friction and wear rates [1]. These are amorphous coatings similar to the continuous random network of amorphous silicon or germanium, in which sp^3 bonding dominates, hence they are referred to as diamond-like [2].

In the case of applications such as automotive engines, increasing the running temperature would also increase the efficiency, thereby reducing energy consumption and carbon footprint. Diamond-like carbon, however, does not perform well as the temperature increases. At ~400 °C a DLC coating begins to graphitise, then oxidise, losing its excellent wear properties as it does so [3]. Other high temperature wear-resistant coating solutions in current development include transition metal dichalcogenides e.g. MoS_2, and ternary metal oxides, but these do not keep their good wear properties across a wide temperature range [4]. Films deposited by the high-power impulse magnetron sputtering (HIPIMS) process [5] have been found to exhibit similarly outstanding room temperature wear behaviour to DLCs [6], and retain this up to higher temperatures [3].

Due to the high energy supplied by incoming ions, coatings grown with the HIPIMS technique experience a great deal of structural rearrangement at the growth surface. The structure of this Mo—W doped C coating is similar to other metal-carbon co-deposited coatings e.g. [7] whilst showing important microstructural differences in the metal incorporation, and shows improved wear resistance under dry sliding

* Corresponding author.
E-mail address: j.sharp@sheffield.ac.uk (J. Sharp).
[1] Present address: University of Strathclyde Glasgow, 16 Richmond Street, Glasgow, G1 1XQ.
[2] Present address: Universiteit Antwerpen, G.U.4112020 Antwerpen Belgium.

https://doi.org/10.1016/j.surfcoat.2019.08.007
Received 4 April 2019; Received in revised form 1 August 2019; Accepted 2 August 2019
Available online 03 August 2019

conditions [6,8]. Composite coatings containing solid lubricant phases are part of the current state of the art e.g. [9], producing good wear properties and a wear surface with inhomogeneity on the micron scale; HIPIMS-produced coatings of the kind investigated here represent a finer (nanoscale), more intimately mixed composite coating that can give an even lower coefficient of friction [8].

These Mo−W coatings have been previously investigated by scanning electron microscopy, Raman spectroscopy and low-magnification transmission electron microscopy (TEM), but not with high spatial resolution electron microscopy. In this study, we explore the fine nanostructure of these Mo-W-C films, and find a complex structure of loosely-ordered rosette-like graphitic clusters 3–8 nm in diameter, which were seen "unrolled" into graphitic solid lubricant in the wear experiments published in [8]. Similar onion-like graphitic clusters were previously seen in Cr−C films co-deposited by steered cathodic arc/unbalanced magnetron sputtering, with a substrate bias voltage of only -95 V [10,7], but are now seen with different metals using HIPIMS and much higher substrate bias. As that Cr−C coating was made with increased substrate bias voltage up to -350 V, it transitioned to a structure of wider layers (~20 nm) of alternating onion-like C clusters and crystalline chromium carbide [11]. This HIPIMS W-Mo-C system, in contrast, displays two regimes of layering simultaneously: layers of clusters, with a secondary modulation in the density of the layers. The second modulation, and the rosette-like graphitic nature of the metal-containing clusters at this higher substrate bias of -500 V, are what set this coating apart from previous metal-doped carbon wear-resistant coatings, made through HIPIMS and otherwise.

In summary, the goal of this study was to take this Mo/W doped carbon coating that performed well in hot wear tests and determine the micro- and nanostructure that allows this property. It transpires that the structure contains features different from previous similar coatings, therefore this study presents details of a new coating microstructure.

2. Material and methods

Carbon films doped with W and Mo were fabricated on M2 grade high speed steel (HSS) using the HIPIMS process [5] in a Hauzer HTC 1000-4 PVD industrial size deposition machine at Sheffield Hallam University. Three graphite targets were operated in unbalanced magnetron sputtering mode and a compound W/Mo target of 200 × 600 mm, with composition ratio W:Mo 1:1, was operated in HIPIMS mode. Samples underwent twofold planetary gear type rotation inside the chamber to achieve maximum possible depth homogeneity; the minimum target to substrate distance was 300 mm. Bias voltage and current at the substrate were −500 V (dropping off during a HIPIMS pulse) and 10A (during the HIPIMS pulse only); details are published in the 2016 patent [12]. The deposition conditions are the same as those reproduced in [13] where extensive characterisation of the plasma was performed.

Before deposition the substrates were ultrasonically cleaned in alkaline water, then ion-etched using the W/Mo HIPIMS target to enhance adhesion of the coating to follow. First a Mo-W-N interlayer was applied using the W/Mo target in a reactive atmosphere of N_2 + Ar, to give minimal residual strain in the coating and better adhesion. The Mo-W-C coating itself was then deposited with chamber pressure of 8 Pa using combined UBM and HIPIMS modes and Ar as a working gas. The mixing ratio between metals:carbon was 1:2. Multiple runs were undertaken using different time-averaged HIPIMS W−Mo target powers; those chosen for investigation by (scanning) transmission electron microscopy used time-averaged power to the HIPIMS target of 2 kW, 4 kW and 6 kW.

TEM samples were prepared by the FIB lift-out technique. A gold coat of 20 nm was sputtered on top of the Mo-W-C coating to mark the original surface in the FIB sections and to minimise charging during sample preparation. Cross-sectional lift-out FIB specimens were then made at Loughborough University using a FEI Nova Nanolab DualBeam FIB. In an attempt to isolate one cluster, when the FIB samples had been thoroughly investigated, the 4 kW sample was sharpened to a thinner edge for periods of ~10s at a time in an FEI Quanta dual-beam FIB at Sheffield University.

TEM imaging was carried out in the JEOL R005 double aberration corrected FEGTEM at Sheffield University operated at 300 kV. Images were obtained using conventional diffraction-contrast TEM, and bright- and annular dark-field scanning TEM (STEM).

Scanning transmission electron microscopy was also performed using the Glasgow JEOL ARM200cF operated at 200 kV. Electron energy loss spectroscopy (EELS) spectrum imaging was performed in Dual EELS mode using a convergence angle of 29 mrad and a collection angle of 36 mrad. The energy loss data on the W-M and Mo-L edges was recorded using a specially optimised camera length to give improved optical transfer at higher energy losses [14]. EELS spectrum images were processed by a procedure similar to e.g. [15] of aligning all spectra in energy using the zero loss peak, trimming excess noisy pixels, removing X-ray spikes, running the low and high loss datasets through PCA to reduce noise [16], and quantifying the data with the Gatan "Elemental Quantification" tool. This tool fits the spectra, taking account of plural scattering, but is purely based on theoretical Hartree-Slater cross sections, not on experimentally measured cross sections, as used in previous Glasgow work ([17];[18]). Unfortunately, suitable standards for this case were not available, so using theoretical Hartree-Slater cross sections was the only sensible option.

Fluctuation electron microscopy (FEM) is generally used to characterise structures with short-range but not long-range order, such as amorphous Si or Ge [19]. The important principle is that each small object, containing short-range crystalline order, contributes an increment of diffracted intensity at the characteristic Bragg diffraction angle for its short-range ordering, but none of them contribute enough intensity to produce a Bragg spot visible above the background. Attempting a dark field image from where the diffraction spot should be would produce an imperceptibly faint image. If, however, a dark field image can be formed from the locus of all the places corresponding to that scattering angle – an annulus at some distance out from the bright field spot – a dark field image can be formed that shows speckled contrast corresponding to all the nanocrystals together. The variance of this dark field image is greater than that of a dark field image from some neighbouring scattering angle that merely receives thermal diffuse scattering, plasmon scattering or other diffuse inelastic scattering. If the variance of these compound dark field images is plotted against scattering angle, peaks will be seen that correspond to the most speckled images, i.e. where the small short-range ordered regions scatter to their Bragg angles. FEM can also be performed in STEM mode, collecting equivalent data and giving equivalent information, through a different but analogous microscope configuration [20].

Fluctuation electron microscopy (FEM) in the STEM mode was performed at Glasgow using the Lorentz STEM mode [21] to give a convergence angle of 0.6 mrad and was recorded as a sequence of diffraction patterns using a camera length of 40 cm to a Merlin for EM (Medipix) detector mounted at the 35 mm camera port (Quantum Detectors Ltd., Harwell, UK). FEM data was processed using the method of [22] whereby an extra convolution with a Gaussian is used as a noise filter in comparison with the original method of Voyles and Muller [20]. Comparisons were made between the resulting variance plot and a number of published crystal structures to determine which candidate crystal structures may have contributed most to the scattering into the speckles in the diffraction pattern.

3. Results and discussion

Films from all three magnetron powers were found to be columnar in microstructure with domed tops at the final film surface (Fig. 1). Total thicknesses of the HIPIMS film above the nitride layer were as follows: 2 kW gave 1.48 μm thickness, 4 kW gave 1.73 μm thickness,

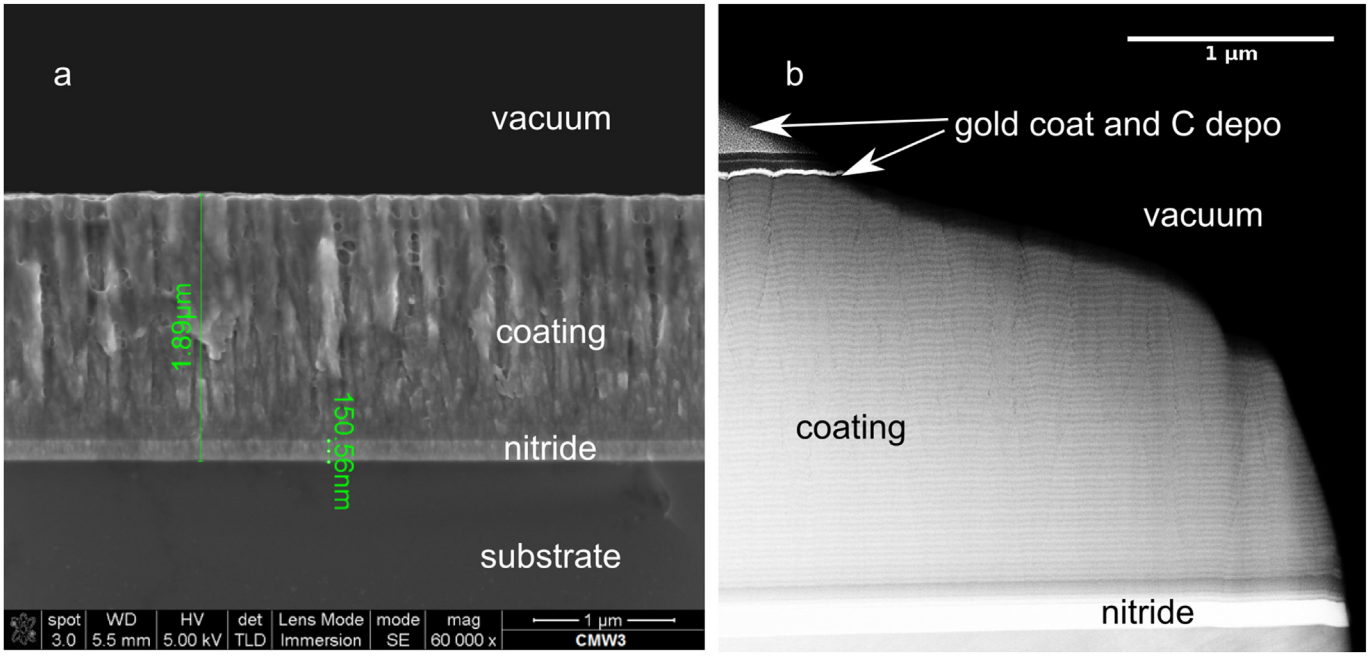

Fig. 1. (a) SEM secondary electron image of 6 kW sample in cross section showing columnar grains. (b) HAADF STEM image of FIB lift-out sample showing columnar grains' boundaries at top and the widest set of stripes.

and 6 kW gave 2.10 µm thickness.

In all films deposited at all three time-averaged powers, the common feature was clusters of higher density - darker in HRTEM and BF STEM, and brighter in ADF STEM – of size 2–8 nm, in a matrix of lower density material. The largest cluster size increased with magnetron mean power: 2 kW produced clusters of 2–3 nm, increasing the time-averaged HIPIMS power to 4 kW and 6 kW pushed the largest cluster size to ~8 nm. The grouping behaviour of the clusters also appeared to change with increasing magnetron power (Fig. 2). The small clusters found in the 2 kW sample had a slight tendency to form rows in places and were isolated from each other. The clusters from 4 kW appeared to have more internal atomic ordering, were more distinguishable from the matrix in contrast, and were joined to each other in a network of no particular shape. From 6 kW, the ordered segments of the clusters were larger in size and formed a greater proportion of the clusters. The ordered parts of the clusters resemble carbon onions [23].

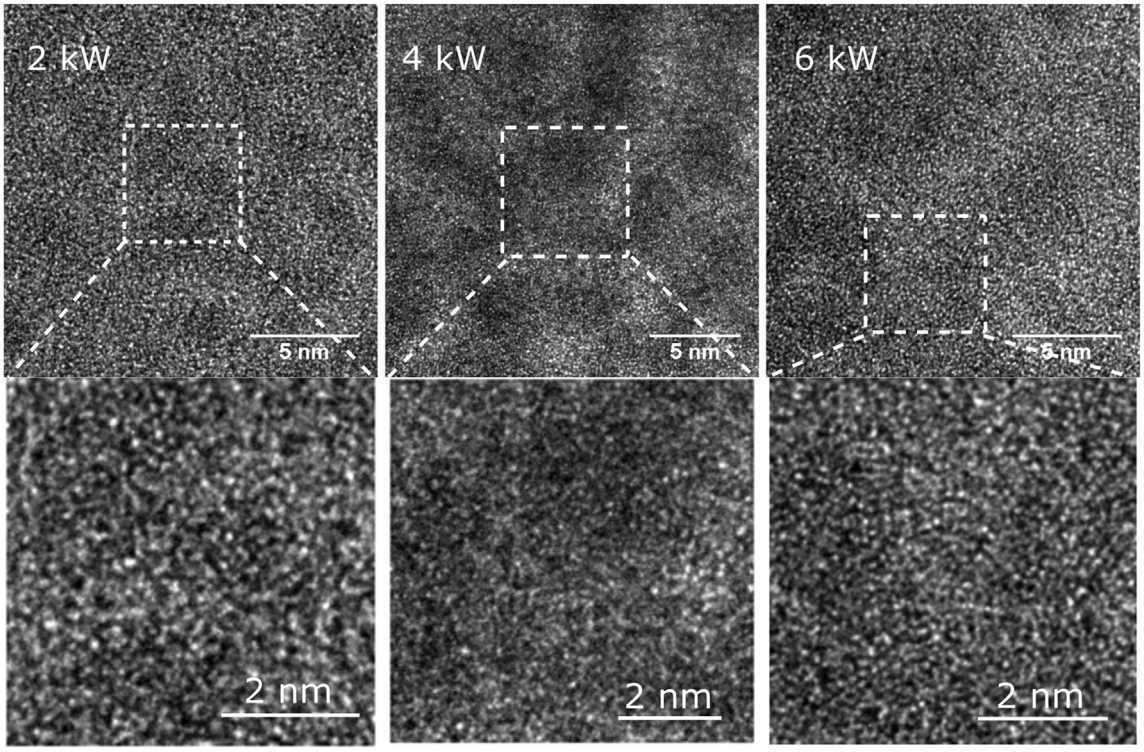

Fig. 2. HRTEM images of clusters in 2 kW, 4 kW and 6 kW samples, with magnified areas below. With increasing magnetron power, the largest clusters are bigger, clusters are more connected, and the structure within them appears more “onion-like”.

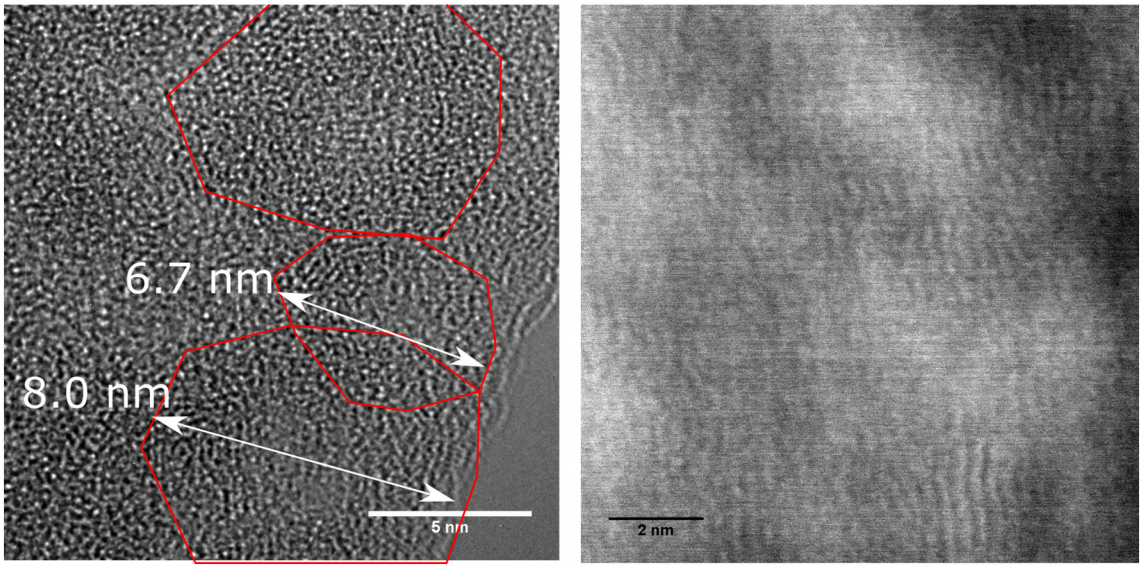

Fig. 3. Left, HRTEM image of clusters at edge of re-thinned 4 kW sample, with approximate cluster boundaries marked by red lines. Right, HAADF-STEM image of clusters at the edge of the re-thinned 4 kW sample, from a different region of the sample. (For interpretation of the references to colour in this figure legend, the reader is referred to the web version of this article.)

The clusters in the 6 kW sample had similar connectivity to the 4 kW sample but are ordered on a slightly larger scale into stripes in a way that will be described below. In all samples the matrix surrounding the clusters appears amorphous.

High-resolution analysis of the re-thinned 4 kW sample (Fig. 3) showed that individual clusters had been successfully isolated at the sample edge. In an area where individual clusters appeared to have been sectioned, HRTEM showed the clusters to be have fringed borders around a core of non-fringed material.

In HAADF-STEM, where the intensity at a position is approximately proportional to atomic number Z^2 [24,25] for high enough scattering angles the clusters show up much brighter than the matrix. The ratio of Z for the elements C:Mo:W is 6:42:74 so the intensity contributing to the HAADF image from each of these elements could be expected to be in a ratio close to 1:49:152 for Z^2 (if all were in equal proportions). The HAADF-STEM contrast should therefore be dominated by the W with some significant contribution from the Mo, but the C almost invisible. The brightness of the clusters in medium magnification ADF STEM images, then, should indicate that the transition metals are mainly segregated there. The fact that the C-rich areas are still visible suggests that there is much more C present than W or Mo, on average. In the re-thinned 4 kW sample, ADF STEM images of a single-cluster thick region (expected to show the W and Mo atoms strongly) show faint fringes around the edges of the cluster and indistinct contrast in the centre – implying that the W and Mo are incorporated in the fringed material around the cluster sides.

Moving a little further into the re-thinned 4 kW sample, the fringe contrast becomes stronger, suggesting that the graphitic material may bridge between one cluster and another. The fringe spacing in the graphitic material was measured to be 0.33 nm, surprisingly close to the spacing of 0.34 nm (c/2) between layers in ABA-stacked graphite [26]. A previous study on nanocrystalline graphite ("graphon") found a layer spacing of 0.347 nm [27]. Studies of bulk graphite intercalation compounds with transition metals have found unexpected patterns: intercalating with Fe gave a layer spacing of 0.59 nm corresponding to that expected with van der Waal's bonding, but Mo gave a layer spacing of 0.37–0.40 nm due to possible ligand-like behaviour; the spacing in a W intercalation compound from that same study could not find an interlayer spacing by XRD because the compounds were "apparently highly disordered" [28]. Interpreting interlayer spacings measured in these clusters may therefore be far from straightforward.

The clusters are also arranged differently on the medium length scale. In the 2 kW sample, stripes are faintly visible along the film normal direction with spacing ~22 nm (Fig. 4a), but it is not clear what causes this striped contrast. These stripes in the 2D image translate in 3D to layers in the coating formed over time during growth. The 4 kW sample (Fig. 4b) also showed these faint stripes, with spacing 17.8 nm, but also a finer regime of stripes of spacing ~6.1 nm with stronger contrast which approximately occur at 3 finer stripes per cycle of coarse stripes (Fig. 4c). This corresponds to each finer stripe being a single layer of clusters. At the bottom of the 4 kW film – corresponding to the beginning of growth – the coarse stripes are more intense and irregular, as if the events causing the stripes were just becoming established (Fig. 4).

The sample made with 6 kW magnetron power shows the most developed striations. Coarse striations are stronger and with spacing ~33 nm, fine stripes have spacing ~6.8 nm, with 4–5 fine stripes per coarse stripe. It is possible to see more detail about the origin of this striped contrast in this sample. The clusters are arranged in lines perpendicular to the growth direction, but appear disordered in position within the lines – these are the fine stripes. The coarse stripes can be seen as a modulation in the breadth of the fine stripes and the density of the material between the clusters; possibly therefore a modulation of the degree of cluster development with depth (Fig. 5). In this 6 kW sample too there is an area at the base of the coating that is not the same as the following material, as if the pattern was still establishing itself.

One possible source of the two sets of stripes is from the twofold rotation of the substrate within the deposition chamber, which brings it closer and further away from the HIPIMS Mo/W target, modulating the rate of Mo/W deposition and the energy input to the substrate allowing self-organisation of the mobile atoms in the growing film, by a mechanism that is not yet clear until the structure of the clusters is further clarified. A combination of the diameter and gearing of the two sets of turntables produces a small diameter rotation that has frequency 3.66 times higher than that of the larger rotation [29]; therefore, if both stripes are produced by the rotations, they should have a ratio of 3.66 between their spacings. This is possible in the case of the 4 kW sample (Fig. 4c) in which the larger periodicity covers between 3 and 4 of the smaller intensity cycles. The 6 kW sample (Fig. 5a), however, shows a ratio of 4–5 between the wider and narrower periodicities.

The location of cluster formation can be clarified; a brief literature

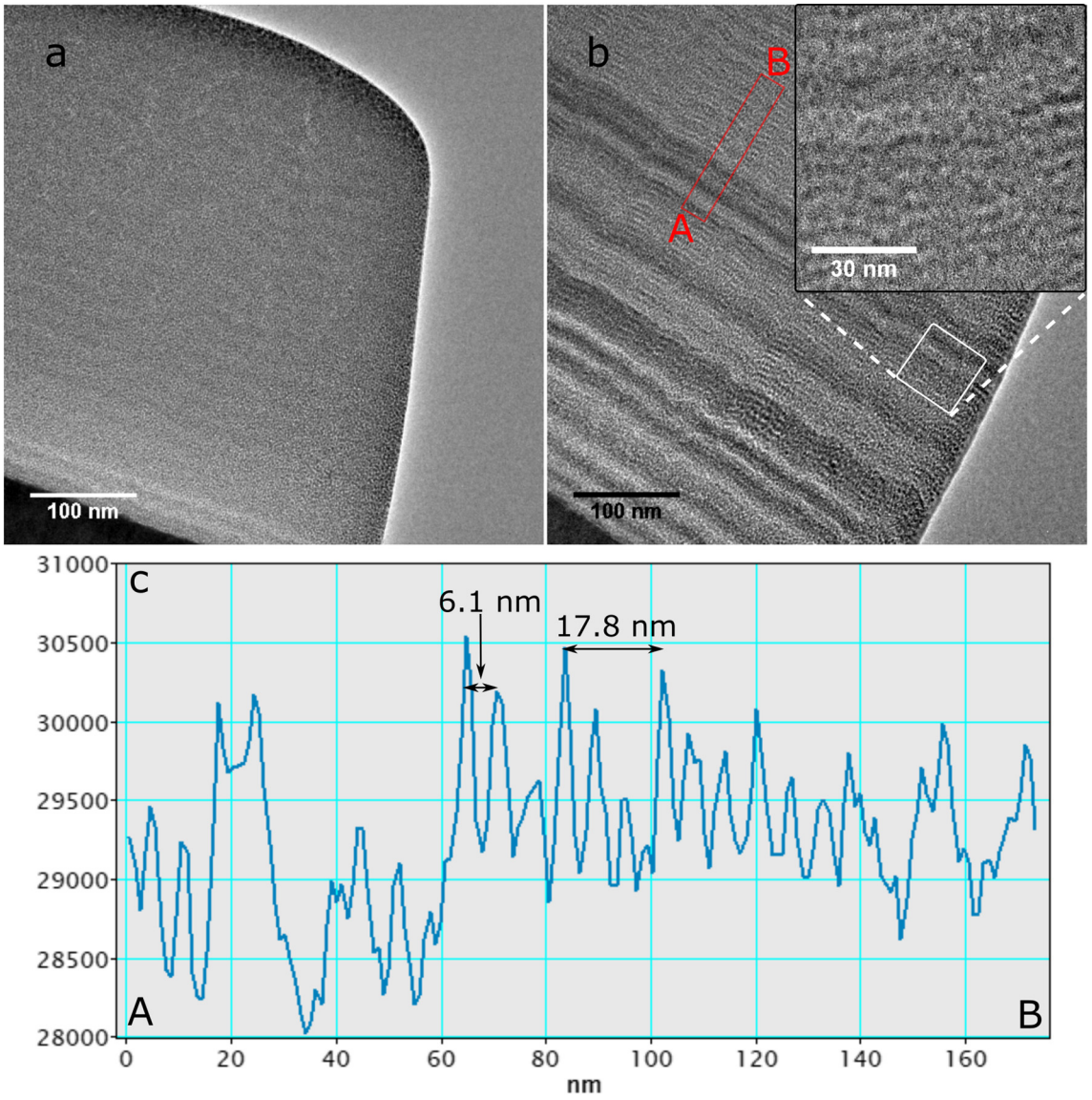

Fig. 4. (a) Lower magnification TEM image of 2 kW sample showing faint, coarse stripes. (b) Similar image for 4 kW sample showing uneven coarse stripes at bottom. Inset b: fine stripes from the indicated region. (c) Line profile from the indicated region of (b) to measure stripe spacings; capitals A and B indicate correspondence between line on image and profile.

search finds penetration depths after a single W ion implantation into amorphous carbon of ~30 nm for 60 keV W ions [30] and a similar depth for 20 keV W ions [31]. Monte Carlo modelling in SRIM/TRIM software [32] (www.srim.org) of 0.5 keV W ions into amorphous carbon gives a range of 2.7 nm with straggle of 0.5 nm. The formation site for clusters should therefore be considered as a short distance below the surface the metal ions' interaction volume is involved with making the top one or possibly two fine stripes in the growing film.

Increasing the mean power supplied to the HIPIMS target should increase the density of metal Mo and W ions available to bombard the substrate with, but not the energy with which each ion impacts the substrate [32]. The substrate at 6 kW time-averaged power should therefore have more W and Mo delivered to the ~3 nm formation stripe.

It is therefore plausible that by the time the substrate on the turntable is brought around to face the HIPIMS target, the W and Mo implanted during the last rotation have not yet all assembled into clusters, and are still relatively available for cluster formation in the top ~3 nm of the film. These would add to the next influx of metal ions to make an even higher excess of metal ions in the top of the film. A larger number of clusters are formed closer together in the next layer of clusters to accommodate the higher W and Mo concentration on the growing surface: this stripe is darker than the previous one.

This would merely result in progressive densifying of the cluster distribution as the film grew, which is not what is seen here. One cannot infinitely increase the concentration of clusters in a layer; they will impinge on one another. The layer may then become a small heap, with extra clusters piled on top but still in a disordered way. This would present as a wider, even denser layer. The excess of Mo and W would then be accommodated by this “heap layer” and the concentration of metal atoms for the next layer would not be excess; a longer-period cycle would begin again. The 6 kW coating, accumulating a larger excess of Mo/W at the growth surface, may form two adjacent heap layers, thus extending the wider modulation period. This would also explain the two or more highest-intensity layers per wide-period modulation seen in the line profile of 6 kW HAADF-STEM image Fig. 5. This hypothesis on the origin of the wider-period modulation could be tested by taking TEM specimens in the plane of the film, to observe the 3D arrangement of clusters within a layer. Changing the time-averaged HIPIMS target power mid-run during deposition as done in [11] would

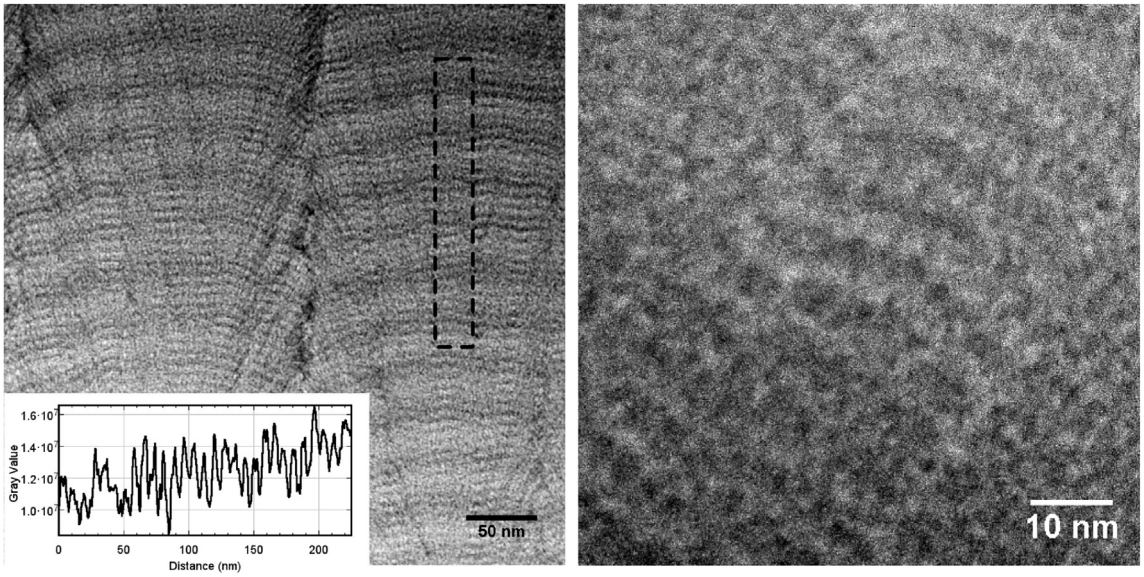

Fig. 5. Left, HAADF STEM image of 6 kW coating, with line trace from dotted region inset. Right, TEM image showing arrangement of clusters within two-stripe microstructure.

also provide useful data.

3.1. Microanalysis of clusters

To assess whether the clusters differed from the matrix chemically as well as in ordering, rough spot EDS and EELS analysis was undertaken. A problem is met here in terms of projection. If the clusters are at most 8 nm across, then the thickness of the initial FIB sample at a point could contain 5–15 clusters. Microanalysis of a spot that looks like "a cluster" can then be sampling 10 clusters, plus the matrix material in between them – so the materials being analysed are not cluster and matrix, but (cluster + matrix) and matrix. This should be more problematic in the lower magnetron power coatings, in which the clusters are less strongly segregated into the stripes, because there is less difference between the cluster-rich and cluster-poor parts, so all points sampled will be (cluster + matrix) in less different proportions. This was the primary motivation behind re-thinning the 4 kW sample to isolate single clusters. Only the EELS analysis from the re-thinned sample is presented here, because the initial rough analysis before re-thinning provided a fraction of the same information as the analysis after re-thinning.

Fig. 6 shows background-subtracted, deconvolved EELS edges for (a) the C—K edge region, (b) a wider energy range from 200 to 800 eV, and (c) a higher-loss energy range covering the W-M and Mo-L edges, all taken across a thin region of clusters and carbon. The carbon K-edge is moderately similar to that from an evaporated amorphous carbon standard (acquired separately in Glasgow), but the π^* peak is slightly stronger, suggesting that this material is a little more graphitic in character than our standard (although nowhere near as well ordered as a well-crystallised graphite) – no significant difference was seen in C—K edges recorded on or off clusters. This is probably due to the thickness of most specimen areas – that with few nm clusters in a specimen 10s of nm thick, all areas will give spectra containing both metal clusters and carbon matrix, and the carbon matrix dominates by volume. The C—K edge is preceded by a rise related to the Mo-$M_{4,5}$ edge (227 eV) and the W—$N_{4,5}$ edge (245 eV). After the C—K edge, small edges for Cr-$L_{2,3}$, Fe-$L_{2,3}$, and a very small one for Co-$L_{2,3}$ are also seen.

The presence of reasonable amounts of Fe, Cr and Co in the clusters is unexpected. If they were only present at the bottom of the film, this could be explained by intermixing caused by the energetic ion flux; however, they are present at points far from the substrate/film interface (also seen in EDS spectra). Another possibility is that Fe, Co and Cr were redeposited during FIB sample preparation; the FIB ion beam passes over the sample from the top of film towards the substrate, however, so redeposition would be expected more in the opposite direction. The remaining possibility is that these elements are present in the deposition chamber at low concentrations, sputtered from components in the chamber, most likely impurities in the W/Mo target and/or the support bracket for the target. In the optical emission spectra of the plasma in the chamber measured during deposition of a similar film, shown in [13], there are additional peaks as well as W, Mo and Ar. These can be attributed to minor peaks from Fe or Cr. Unfortunately, the regions of the spectrum that contain the key Fe and Cr optical emission peaks were omitted when their spectral range was set to receive W, Mo and Ar peaks. The data that is present, however, suggests strongly that Fe and Cr in the clusters originates from target contamination in the deposition chamber.

Fig. 7 shows EELS maps from a DualEELS spectrum image of the very thinnest region next to the edge of the 4 kW sample covering the Mo-M, W—N, C—K, Cr-L, Fe-L, Co-L and W-M edges. Seeing as the Mo-M and W—N edges overlap, the first map does not absolutely separate out these two elements. In the higher loss range, the W-M and Mo-L edges are clearly seen and easily separated; the W-M map from the same dataset clearly shows W alone (please note some drift occurred between the maps and the step size was larger for the high energy edges, because a longer dwell time was needed for each pixel).

The EELS maps show that the clusters contain carbon and are also enriched in all the metallic elements, whereas the surrounding matrix is metal poor and carbon-rich. This was checked by point EELS and EDS spectra taken from clusters and from stripes between clusters. A second pair of maps is shown from a higher loss dataset covering the same pair of slightly larger clusters in a very thin area. These were recorded at twice the pixel size with a longer counting time to ensure a useable signal to noise ratio at the high losses needed for W-M and Mo-L edges, and unambiguously demonstrate that the clusters contain both W and Mo.

Quantification was performed at a few individual points in these spectrum images and just to demonstrate the extremes of this, two points were selected from this super-thin region; results are shown in shown in Table 1. This shows that the clusters are rich in both the Mo and W, as well as also picking up some Cr and Fe from target contamination. On the other hand, the C-rich matrix surrounds all the

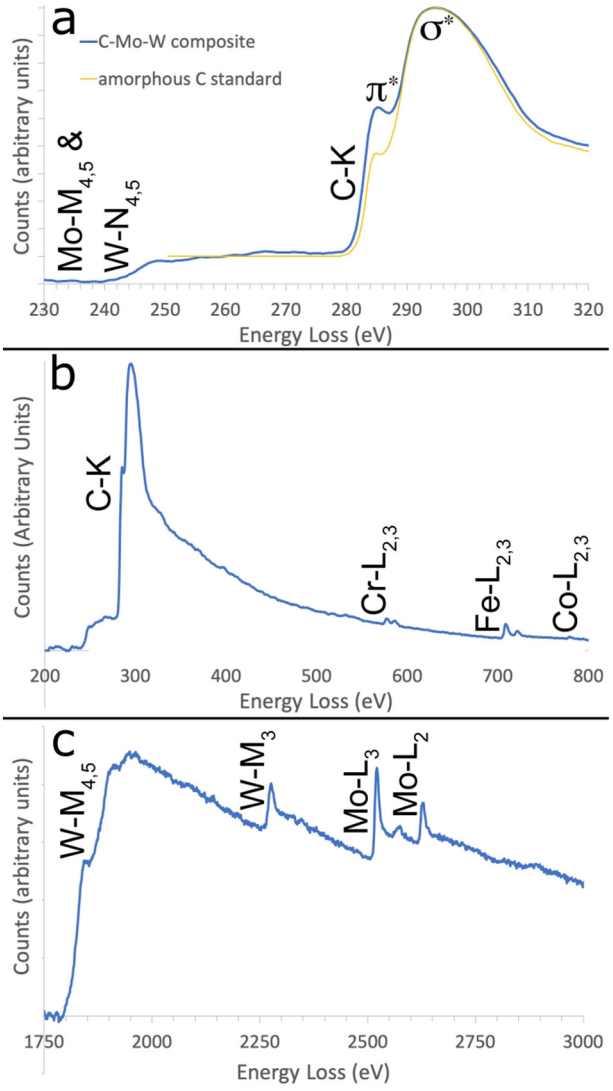

Fig. 6. Background-subtracted and deconvolved EELS spectra from one region close to the edge in 4 kW sample. (a) C−K edge region; (b) from 200 to 800 eV containing the C−K edge region; (c) deep core-loss region to record W-M and Mo-L edges.

clusters. Whilst the lower loss dataset makes the separation of Mo from W difficult and the quantification of the Mo-M/W−N combined edge is difficult to trust, it is clear that the clusters are around 1:1 in their W:Mo ratio from the higher loss dataset. Interestingly, the matrix, although about 85at% C, contains a higher W:Mo ratio of nearer 2:1, even in very thin areas like that which was used for this analysis, suggesting that some W goes into the C matrix, whereas less Mo does so.

In summary, we would describe the coating as an amorphous carbon matrix with small amounts of Mo and W, containing clusters of semi-ordered material consisting of approximately 50% C and 50% metals (Mo, W, Cr, Fe).

3.2. Fluctuation transmission electron microscopy

FEM plots determined from low convergence angle STEM data from the 2, 4 and 6 kW samples are shown in Fig. 8. Both Fig. 8a (upper) and Fig. 8b (lower) show the same FEM data of variance versus $q = 2\pi/d$, where d is the crystal plane spacing. They are compared with two different sets of model reference values, calculated using CrystalMaker X, (CrystalMaker Software Ltd., Oxford, UK), which are depicted separately on the two instances of the plot. Fig. 8a compares the data with

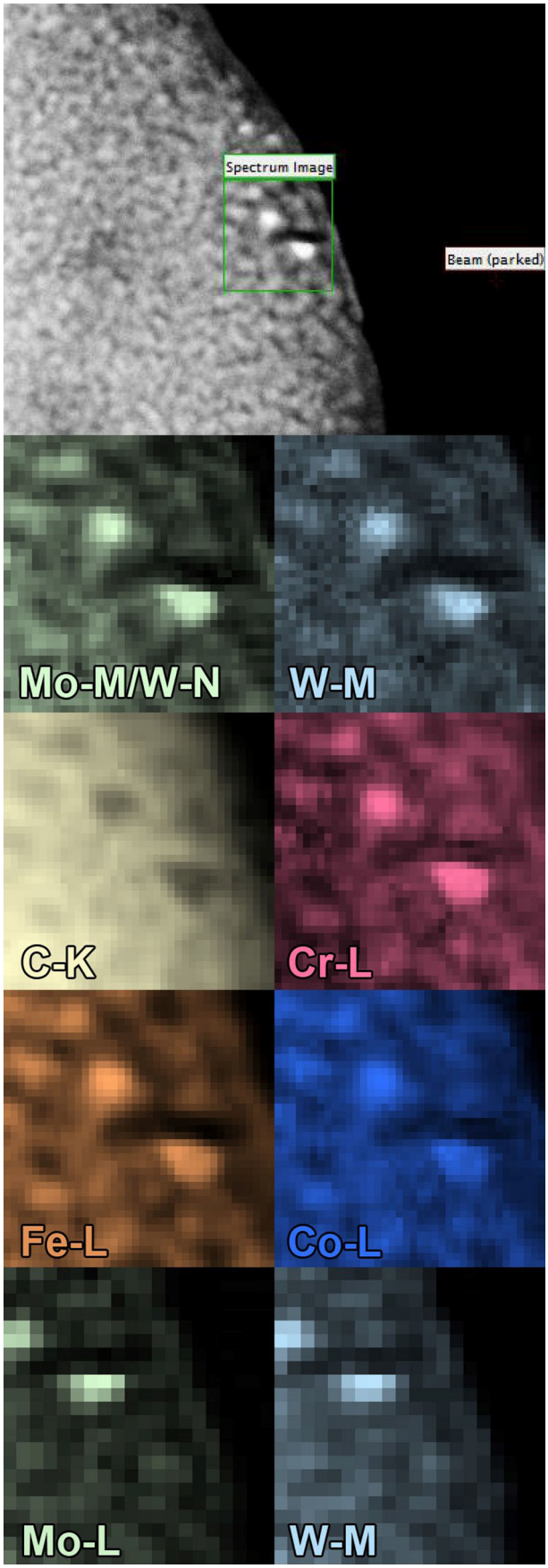

Fig. 7. EELS spectrum imaging maps of clusters in the re-thinned 4 kW sample.

Table 1
Standardless quantification of clusters and matrix using standard routines in Gatan Digital Micrograph. The first seven columns are from one spectrum image, whereas the last two are from a separate spectrum image of the same area, but covering the higher loss edges at good signal to noise ratio. Units are at%. The W-M/Mo-L section to the right is derived from just those two edges in the higher-loss EELS spectra; the main section is from the wide 200-800 eV spectra.

Area	C	Mo-M/W-N	O	Cr	Fe	Co	W-M	W-M	Mo-L
Cluster	47.6	9.5	0.0	4.7	14.0	7.6	16.6	45.5	54.5
Matrix	84.9	1.0	1.4	1.3	4.2	3.7	2.7	64.2	35.8

the diffractogram peak positions from crystal plane spacings that would exist for some different crystalline structures including diamond, graphite, β-Mo_2C and WC. This is the generally accepted way to evaluate FEM data. Fig. 8b compares the data with simple interatomic spacings r, rather than crystal plane spacings, of the same structure, in the form $2\pi/r$; this disregards systematic absences. In both 8a and 8b, the heights of the reference lines are proportional to the multiplicity of the spacings. Hexagonal WC [33] and MoC have almost identical structures and lattice parameters, such that WC can be used as a proxy for both in this discussion. Interatomic spacings are not normally used to evaluate FEM data when scattering is known to be from clusters that are structurally similar to nanocrystals of a known crystal structure. In this case, however, we do not know that we are looking only at crystals of diamond, graphite, Mo_2C and WC; there may also be different, non-equilibrium structures present due to the high energy of incident Mo and W ions available during film deposition. The interatomic spacings are therefore separately considered in order to test the hypothesis that the structure may be highly disordered and the main diffraction events come from interatomic distances alone.

The dependence of FEM normalised variance on atomic number is relevant to this system. According to Liu et al. [34], the normalised variance produced by a pair of scatterers/lattice planes of atoms A and B should be weighted by combinations of atomic scattering factors: f_A^4, $f_A^3 f_B$, $f_A^2 f_B^2$, $f_A f_B^3$, f_B^4. Electron atomic scattering factors are proportional to atomic number Z [35], so the shape of the variance plot should depend most strongly on spacings between the higher Z atoms W and Mo. This means, in contrast to the EELS, where pure numbers of atoms lead to carbon dominating the spectra, to a situation in FEM where the metal-carbon clusters will dominate the results. Carbon, however, may still make a strong contribution through sheer numbers of atoms.

The most striking region of the FEM data is the strong, narrow peak at ~2.5 $Å^{-1}$ labelled as A. The scattering vector, q, from the $\{10\bar{1}0\}$ plane spacing of hexagonal WC falls in this position, which is known to be the strongest peak in a diffractogram of WC. The next feature of interest is the pair of wide peaks at smaller q (wider spaced atoms/planes), marked B1 and B2. The 4 kW film has two peaks of similar height, B1 and B2; the 2 kW film has one broad peak closer to B1; the 6 kW has B2 stronger. Peak B1 does not match any lattice plane spacings. Peak B2 matches the {0002} interlayer crystal plane spacing in graphite [36]. This implies that the 6 kW and 4 kW film contain nanocrystals of graphite, but the origin of peak B1 is not explained by any lattice plane spacings from the expected candidates, although intercalation structures and highly disorder graphites can have larger plane spacings, which would extend peaks in variance to lower q.

Thirdly, there is detail in the higher-q region (c). In terms of crystal plane spacings, the WC $\{11\bar{2}0\}$ plane spacing matches a broad peak in all three FEM variance plots at ~4.3 $Å^{-1}$. There are also plane spacings from Mo_2C [37] in this region that appear aligned with the small waves in the 6 kW plot and to some extent the 4 kW plot. This implies that in the two higher power films, carbide structures are also present, at least in terms of the basal planes of the hexagonal WC structure.

It is also instructive to note what is **not** so clearly interpretable. If peak A at ~2.5 $Å^{-1}$ originates from the $\{10\bar{1}0\}$ planes of hexagonal WC, then the crystal plane spacings {0001} and $\{10\bar{1}1\}$ from hexagonal WC should also be present at ~2.2 $Å^{-1}$ and ~3.3 $Å^{-1}$ respectively. The first may contribute to the breadth of the peak around 2.5 $Å^{-1}$. The second is less clear but, may contribute to the broad ridge of variance between 3.1 and 4.5 $Å^{-1}$. However, WC plane spacings perpendicular to {0001} appear to influence the FEM plot to the greatest degree. This may be similar to recent work on highly disordered graphites [38], where the (0002) diffraction ring dominates.

The {111} crystal plane from diamond does not correspond to any FEM peaks, indicating that diamond nanocrystallites are not present. The second-nearest-neighbour interatomic spacing at 2.5 $Å^{-1}$ aligns with peak A, and the further neighbour spacings are in the lower-Q region with many spacings from other candidate structures. The FEM data therefore indicates amorphous carbon rather than nano-diamond is present, as expected. This is also in accord with the EELS data of Fig. 6 showing that the carbon is more graphitic than diamond-like.

This suggests there may be some hybrid graphite/WC (and MoC) intercalation type structure, with interlayer spacings dominated by graphite. Simulation work is planned to test if this could plausibly explain the various data obtained.

Another discrepancy is that peak B1 at ~1.5 $Å^{-1}$, found in the 2 kW and 4 kW coatings, does not correspond to any crystal plane spacings in the candidate structures considered here; it does, however, match some interatomic spacings that are not diffracting planes. Of the two most populous, the first is graphite $\frac{1}{3}[4\bar{2}\bar{2}3]$, that is, across one hexagon to the second-nearest neighbour and then up to the next layer. Also in the B1 region of the plot is the $\frac{1}{3}[\bar{1}2\bar{1}3]$ distance in WC – the W atoms would be the main contributor here. For these interatomic spacings out of the basal plane to become non-forbidden through symmetry breaking, but the out-of-basal-plane WC{0001} and WC$\{10\bar{1}1\}$ crystal spacings to be unseen in the FEM data, implies that we do not have WC, but some structure with WC basal planes and graphite basal planes. A good starting estimate for future modelling of the structure in these onion/rosette-like clusters may be WC and graphite basal planes staggered with respect to each other in a way that reproduces the graphite $\frac{1}{3}[4\bar{2}\bar{2}3]$ and WC $\frac{1}{3}[\bar{1}2\bar{1}3]$ distances in a form of best-fit structure.

If interatomic spacings become admissible, we may also attempt to interpret the shift to higher q in peak A seen in the 2 kW sample's FEM data. The 2 kW sample's instance of peak A fits better the graphite second-nearest-neighbour in-plane spacing $\frac{1}{3}[2\bar{1}\bar{1}0]$ than the WC$\{10\bar{1}0\}$ plane spacing that fits the 4 kW and 6 kW so well. Correspondingly, the peak at ~4.5 $Å^{-1}$ in the 2 kW data aligns well with the graphite interatomic spacing at that value, which is the nearest neighbour in the graphite hexagon. These two graphite in-plane neighbour spacings becoming un-forbidden would imply the graphitic symmetry in the 2 kW film is broken/not formed, which may follow given that there is a lower density of W/Mo ions meeting the coating growth surface at the lowest HIPIMS power and causing the onion-like structure to develop.

There is a great deal of information contained in the FEM data here, and future work to explore these potential cluster structure ideas in conjunction with other techniques such as Raman scattering would be essential to untangling these complex questions. Nevertheless, the clear conclusion from the FEM is that the short range atomic structure of the clusters is likely related to that of (W,Mo)C.

4. Conclusions

Thin films of C/Mo/W deposited using combined unbalanced magnetron (UBM) sputtering/high-power impulse magnetron sputtering (HIPIMS) were studied by HRTEM, fluctuation electron microscopy, STEM and TEM microanalysis in an aberration-corrected instrument. Combined STEM and HRTEM found 2–8 nm structures that resemble graphitic “onions” with the metal atoms arranged regularly within them. EELS mapping showed the clusters to be richer in Mo and W than the matrix. With increasing time-averaged HIPIMS power, clusters become slightly larger, and arranged into layers with

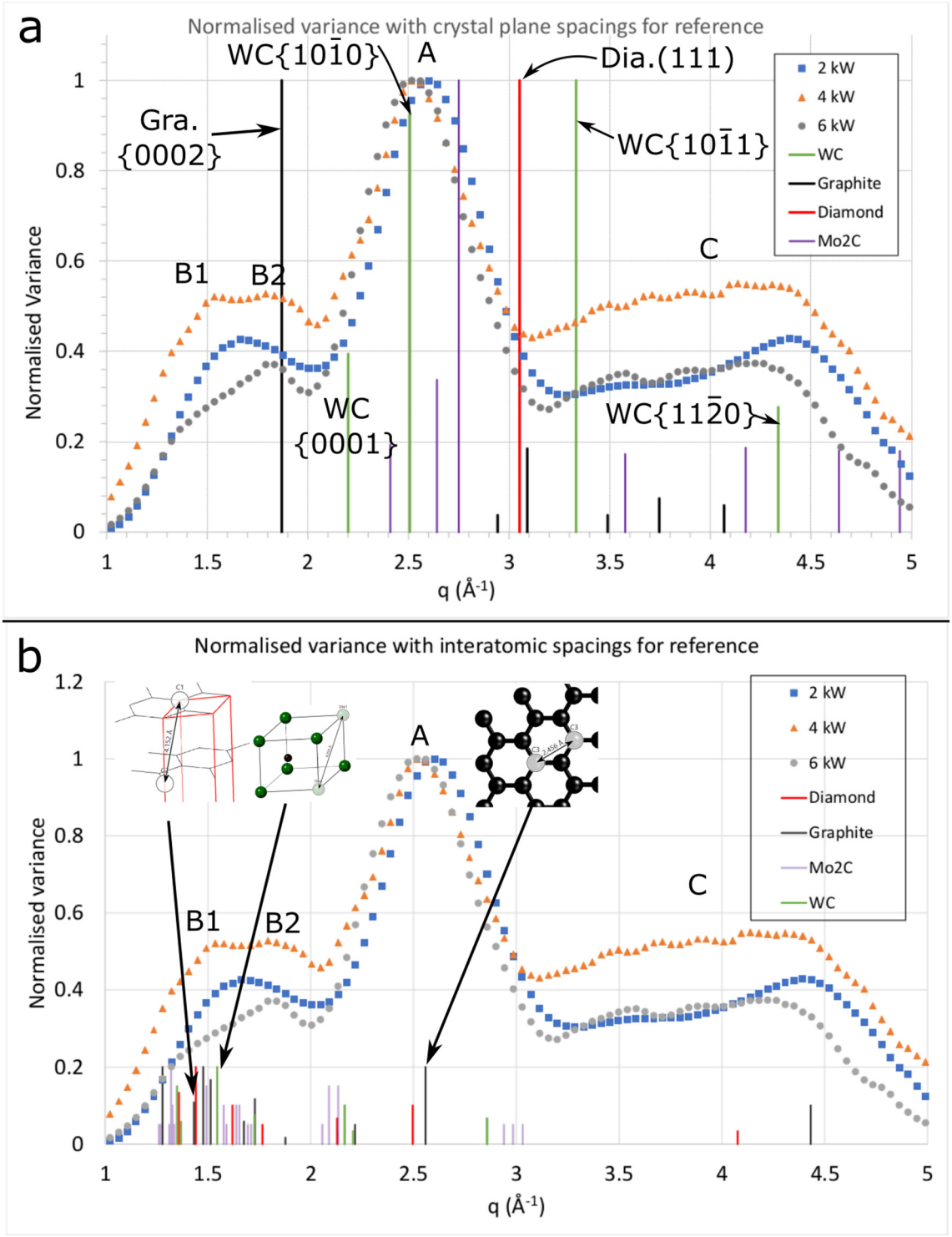

Fig. 8. Normalised variance plots from fluctuation microscopy of the 2 kW, 4 kW and 6 kW samples with reference peak positions shown for Mo_2C, WC, graphite and diamond. The two plots show the same data against different reference data: in 8a, comparison is drawn with crystal plane spacings; in 8b, comparison is drawn with interatomic spacings. The interatomic spacings in the bottom image are normalised to 0.2 to avoid obscuring the variance plot.

amorphous matrix between them; films from 4 kW and 6 kW mean power showed a coarser meta-layering in the form of a modulation of the degree of ordering of the finer layers. This meta-layering is related non-straightforwardly to the substrate rotation in the deposition chamber.

Fluctuation electron microscopy variance plots were dominated by a spacing similar to that for the basal plane of the hexagonal WC-type structure for all films. Additionally, the 2 kW and 4 kW films contained structures with some graphite/graphene-like basal plane spacings but not the layered crystalline structure of graphite; the 4 kW and 6 kW films showed indications of layered graphite nanocrystals and possible β-Mo_2C type structures.

Acknowledgements

J.S. thanks the Mercury Centre at the University of Sheffield for

funding, which was part funded by the ERDF under grant MERCURY – 904467. I.C.M. acknowledges support from CONACyT and RobertoRocca Education Fellowship. We gratefully acknowledge funding from EPSRC for the pixelated STEM detector and the software used in its operation for the fluctuation microscopy (EP/M009963/1, EP/K503903/1 & EP/R511705/1). AD was supported by the EPSRC CDT in Integrative Sensing and Measurement, Grant Number EP/L016753/1. Funding sources did not influence the planning or execution of this work except to enable it.

References

[1] K. Bewilogua, D. Hofmann, History of diamond-like carbon films — from first experiments to worldwide applications, Surf. Coat. Technol. 242 (2014) 214.
[2] A. Erdemir, C. Donnet, Tribology of diamond-like carbon films: recent progress and future prospects, J. Phys. D. Appl. Phys. 39 (18) (2006) R311.
[3] P. Mandal, A.P. Ehiasarian, P.E. Hovsepian, Isothermal and dynamic oxidation behaviour of Mo–W doped carbon-based coating, Appl. Surf. Sci. 353 (2015) 1291.
[4] H. Torres, M. Rodrigues Ripoll, B. Prakash, Tribological behaviour of self-lubricating materials at high temperatures, Int. Mater. Rev. 63 (5) (2017) 309–340.
[5] V. Kouznetsov, K. Macák, S.J. M, H. U, A novel pulsed magnetron sputter technique utilizing very high target power densities, Surf. Coat. Technol. 122 (1999) 290.
[6] P. Mandal, A. Ehiasarian, P. Hovsepian, Tribological behaviour of Mo − W doped carbon-based coating at ambient condition, Tribol. Int. 90 (2015) 135.
[7] Z. Zhou, W.M. Rainforth, M.H. Gass, A. Bleloch, A.P. Ehiasarian, P.E. Hovsepian, Cr/C nanocomposite coating deposited by magnetron sputtering at high ion irradiation conditions, J. Appl. Phys. 110 (2011) 073301.
[8] I.C. Müller, J. Sharp, W.M. Rainforth, P. Hovsepian, A. Ehiasarian, Tribological response and characterization of Mo-W doped DLC coating, Wear 376 (April 2017) 1622.
[9] Z.-C. Feng, Y.-F. Liu, Y. Li, G.-B. Sun, Z. Zhang, C.-X. Shi, Microstructure and high temperature reciprocating sliding wear properties of MoSi2/TiC/gamma-Ni composite coating in-situ synthesised by co-axial powder feeding plasma transferred arc cladding, Tribol. Int. 129 (2019) 82–91.
[10] P.E. Hovsepian, Y.N. Kok, A.P. Ehiasarian, A. Erdemir, J.-G. Wen, I. Petrov, Structure and tribological behaviour of nanoscale multilayer C/Cr coatings deposited by the combined steered cathodic arc/unbalanced magnetron sputtering technique, Thin Solid Films 447–448 (2004) 7–13.
[11] P.E. Hovsepian, Y.N. Koki, A.P. Ehiasarian, R. Haasch, J.-G. Wen, I. Petrov, Phase separation and formation of the self-organised layered nanostructure in C/Cr coatings in conditions of high ion irradiation, Surf. Coat. Technol. 200 (5–6) (2005) 1572–1579.
[12] P. E. Hovsepian, D. Doerwald and R. Tietema, "Coating and method for its deposition to operate in boundary lubrication conditions and at elevated temperatures". Europe Patent EP2963145A1, 6th January 2016.
[13] W. Gajewski, A.P. Ehiasarian, M. Żelechowski, P.E. Hovsepian, Composition and dynamics of high power impulse magnetron discharge at W-Mo-C target in argon atmosphere, Surf. Coat. Technol. 327 (2017) 185–191.
[14] A.J. Craven, H. Sawada, S. McFazdean, I. MacLaren, Getting the most out of a post-column EELS spectrometer on a TEM/STEM by optimising the optical coupling, Ultramicroscopy 180 (2017) 66–80.
[15] K.J. Annand, I. MacLaren, M. Gass, Utilising DualEELS to probe the nanoscale mechanisms of the corrosion of Zircaloy-4 in 350 degrees C pressurised water, J. Nucl. Mater. 465 (2015) 390–399.
[16] G. Lucas, P. Burdet, M. Cantoni, C. Hebert, Multivariate statistical analysis as a tool for the segmentation of 3D spectral data, Micron 52-53 (2013) 49–56.
[17] A.J. Craven, J. Bobynko, B. Sala, I. MacLaren, Accurate measurement of absolute experimental inelastic mean free paths and EELS differential cross-sections, Ultramicroscopy 170 (2016) 113–127.
[18] A.J. Craven, B. Sala, J. Bobynko, I. MacLaren, Spectrum imaging of complex nanostructures using DualEELS: II. Absolute quantification using standards, Ultramicroscopy 186 (2017) 66–81.
[19] M.M.J. Treacy, J.M. Gibson, L. Fan, D.J. Paterson, I. McNulty, Fluctuation microscopy: a probe of medium range order, Reports of Progress in Physics 68 (2005) 2899.
[20] P.M. Voyles, D.A. Muller, Fluctuation microscopy in the STEM, Ultramicroscopy 93 (2) (2002) 147–159.
[21] S. McVitie, D. McGrouther, S. McFazdean, D.A. MacLaren, K.J. O'Shea, M.J. Benitez, Aberration corrected Lorentz scanning transmission electron microscopy, Ultramicroscopy 152 (2015) 57–62.
[22] M.J. Hart, R. Bassiri, K.B. Borisenko, M. Veron, E.F. Rauch, L.W. Martin, S. Rowan, M.M. Fejer, I. MacLaren, Medium range structural order in amorphous tantala spatially resolved with changes to atomic structure by thermal annealing, J. Non-Cryst. Solids 438 (2016) 10–17.
[23] L.-C. Qin, S. Iijima, Onion-like graphitic particles produced from diamond, Chem. Phys. Lett. 262 (1996) 252.
[24] S.J. Pennycook, D.E. Jesson, High-resolution Z-contrast imaging of crystals, Ultramicroscopy 37 (1991) 14–38.
[25] S.J. Pennycook, Z-contrast STEM for materials science, Ultramicroscopy 30 (1989) 58.
[26] P. Trucano, R. Chen, Structure of graphite by neutron diffraction, Nature 258 (1975) 136–137.
[27] P.H. Gamlen, J.W. White, Structure and dynamics of microcrystalling graphite, graphon, by neutron scattering, Journal of the Chemical Society, Faraday Transactions 2: Molecular and Chemical Physics (1976) 446–455.
[28] M.E. Vol'pin, Y.N. Novikov, N.D. Lapkina, V.I. Kasatochkin, Y.T. Struchkov, M.E. Kazakov, R.A. Stukan, V.A. Povitskij, Y.S. Karimov, A.V. Zvarikina, Lamellar compounds of graphite with transition metals. Graphite as a ligand, J. Am. Chem. Soc. 97 (12) (1975) 3366–3373.
[29] Z. Zhou, W.M. Rainforth, U. Falke, M. Falke, A. Bleloch, P.E. Hovsepian, On the structure and composition of nanoscale TiAlN/VN multilayers, Philos. Mag. 87 (2) (2006) 1.
[30] H. A, E. P. J, C. D. D and P. P. J. K, Compaction, distribution and chemical bonding of tungsten-implanted glassy carbon, J. Appl. Phys. 72 (1992) 5687.
[31] M. Xu, W. Zhang, Z. Wu, S. Pu, L. Li, P.K. Chu, Evolution mechanism of nanocrystalline tungsten-carbon and effects on tungsten implanted amorphous hydrogenated carbon, J. Appl. Phys. 102 (2007) 113517.
[32] J.F. Ziegler, J.P. Biersack, M.D. Ziegler, SRIM - The Stopping and Range of Ions in Solids, Lulu, (2009).
[33] K. Page, J. Li, R. Savinelli, H.N. Szumila, J. Zhang, J.K. Stalick, T. Proffen, S.L. Scott, R. Seshadri, Reciprocal-space and real-space neutron investigation of nanostructured Mo_2C and WC, Solid State Sci. 10 (2008) 1499–1510.
[34] A.C.Y. Liu, R. Arenal, D.J. Miller, X. Chen, J.A. Johnson, O.Y. Eryilmaz, A. Erdemir, J.B. Woodford, Structural order in near-frictionless hydrogenated diamondlike carbon films probed at three length scales by transmission electron microscopy, Phys. Rev. B 75 (2007) 205402.
[35] D.B. Williams, C.B. Carter, Transmission Electron Microscopy, Springer-Verlag, New York, 2009.
[36] R.W.G. Wyckoff, Crystal Structures, Wiley, 1963.
[37] K. Page, L. Jun, R. Savinelli, H. Szumila, J. Zhang, J. Stalick, T. Proffen, S. Scott, R. Seshadri, Reciprocal-space and real-space neutron investigation of nanostructured Mo_2C and WC, Solid State Sci. 10 (2008) 1499–1510.
[38] P. Lindgren, L. Hallis, F.S. Hage, M.R. Lee, J. Parnell, A. Doye, I. MacLaren, In press, Meteoritics and Planetary Sciences (2019).